Earth and Space Science

RESEARCH ARTICLE
10.1029/2023EA003368

Supercells and Tornado-Like Vortices in an Idealized Global Atmosphere Model

Kai-Yuan Cheng[1,2], **Shian-Jiann Lin**[3], **Lucas Harris**[2], **and Linjiong Zhou**[1,2]

[1]Program in Oceanic and Atmospheric Sciences, Princeton University, Princeton, NJ, USA, [2]NOAA/Geophysical Fluid Dynamics Laboratory, Princeton, NJ, USA, [3]Tianji Meteorological Sciences and Technology Inc., Beijing, China

Key Points:

- The FV3 dynamical core with simple microphysics can simulate individual supercells and cloudy tornado-like vortices at kilometer scales
- A stretched cubed-sphere grid is used to economically reach cloud-resolving scales locally on a real-size Earth
- The dynamics of the simulated tornado-like vortices is consistent with previous studies on tornadogenesis

Supporting Information:

Supporting Information may be found in the online version of this article.

Correspondence to:

K.-Y. Cheng,
kai-yuan.cheng@noaa.gov

Citation:

Cheng, K.-Y., Lin, S.-J., Harris, L., & Zhou, L. (2024). Supercells and tornado-like vortices in an idealized global atmosphere model. *Earth and Space Science*, *11*, e2023EA003368. https://doi.org/10.1029/2023EA003368

Received 23 OCT 2023
Accepted 7 APR 2024

Author Contributions:

Conceptualization: Kai-Yuan Cheng, Shian-Jiann Lin, Lucas Harris
Data curation: Kai-Yuan Cheng
Formal analysis: Kai-Yuan Cheng
Funding acquisition: Shian-Jiann Lin, Lucas Harris
Investigation: Kai-Yuan Cheng, Shian-Jiann Lin, Lucas Harris
Methodology: Kai-Yuan Cheng, Shian-Jiann Lin, Lucas Harris, Linjiong Zhou
Project administration: Shian-Jiann Lin, Lucas Harris
Resources: Shian-Jiann Lin, Lucas Harris

Abstract

We investigate the representation of individual supercells and intriguing tornado-like vortices in a simplified, locally refined global atmosphere model. The model, featuring grid stretching, can locally enhance the model resolution and reach cloud-resolving scales with modest computational resources. Given a conditionally unstable sheared environment, the model can simulate supercells realistically, with a near-ground vortex and funnel cloud at the center of a rotating updraft reminiscent of a tornado. An analysis of the Eulerian vertical vorticity budget suggests that the updraft core of the supercell tilts horizontal vorticity into the tornado-like vortex, which is then amplified through vertical stretching by the updraft. Results suggest that the simulated vortex is dynamically similar to observed tornadoes, as well as those simulated in modeling studies at much higher horizontal resolution. Lastly, we discuss the prospects for the study of cross-scale interactions involving supercells.

Plain Language Summary

We use a simplified global model to study individual supercells and intriguing cloudy rotating winds that behave like tornadoes. This model uses grid-stretching techniques, making it a computationally efficient tool to study supercells on a real-size Earth. Unlike most numerical models of tornadoes which simulate scales of a few tens of meters, our model can realistically simulate supercells and cloudy tornado-like rotating winds even at kilometer scales, which appears unprecedented in the literature. We find that the physics behind the rotating winds is consistent with previous studies, including observations of tornado formation and simulations at much higher resolution. The findings of this study open the door to a better understanding of complex interaction between supercells, tornadoes, and their environment.

1. Introduction

A supercell (an intense convective storm characterized by a single quasi-steady rotating updraft) is often associated with severe weather for its capabilities of producing destructive winds, large hail, extreme precipitation, and dangerous tornadoes. Many field campaigns, such as RELAMPAGO (Remote sensing of Electrification, Lightning, And Mesoscale/microscale Processes with Adaptive Ground Observations; Nesbitt et al., 2021), VORTEX (Verification of the Origins of Rotation in Tornadoes Experiment; Rasmussen et al., 1994), and VORTEX2 (Wurman et al., 2012), provide invaluable data sets for understanding the processes associated with supercells. Those observations, however, are subject to the field of view for a remote sensor or sample size for an in situ instrument. On the other hand, a numerical model can provide a comprehensive picture of a supercell, that is, all variables at every grid cell within a computational domain.

Historically, simulations of supercells were feasible only using limited-area models (e.g., Klemp & Wilhelmson, 1978; Orf et al., 2017; Schlesinger, 1978; Wang et al., 2016) due to the cost of both high temporal and spatial resolutions that are required to resolve the structures and dynamics of supercells on cloud-resolving scales. Nowadays, because of continuing increases in computational capacity, the atmospheric sciences community is ushering in a new era of global cloud-resolving models. Several numerical modeling centers are developing global cloud-resolving models with 2–5 km horizontal resolution that can explicitly resolve deep convection (Cheng et al., 2022; Satoh et al., 2019; Stevens et al., 2019). The ability of a global model to represent deep convection not only reduces the uncertainty caused by cumulus parameterizations (e.g., Stevens & Bony, 2013), but it also paves the way toward a better understanding of multiscale interaction involving convection (e.g., Madden-Julian Oscillation and cloud feedback; Bolot et al., 2023; Zavadoff et al., 2023), which plays an important role in the prediction of convective severe weather at medium-range and longer time scales (e.g., Cheng et al., 2022; Gensini et al., 2020).

Software: Kai-Yuan Cheng, Shian-Jiann Lin, Lucas Harris, Linjiong Zhou
Supervision: Shian-Jiann Lin, Lucas Harris
Validation: Kai-Yuan Cheng
Visualization: Kai-Yuan Cheng
Writing – original draft: Kai-Yuan Cheng, Lucas Harris
Writing – review & editing: Kai-Yuan Cheng, Shian-Jiann Lin, Linjiong Zhou

While this new class of global models has been proven useful for understanding the properties of intense convection on a global scale (Cheng et al., 2022; Harris et al., 2023), these models are at best marginally able to accurately simulate individual supercells. In fact, this group of global models is frequently referred to as global storm-resolving models (e.g., Judt et al., 2021; Nugent et al., 2022).

In this study, we describe an efficient, simplified nonhydrostatic global model, powered by the finite-volume cubed-sphere dynamical core (FV3) developed at the Geophysical Fluid Dynamics Laboratory (GFDL). We use FV3's stretched-grid variable-resolution capability (Harris et al., 2016) and conduct idealized simulations of a supercell at various cloud-resolving scales, ranging from 4 km down to 500 m. The configuration of the simulation is similar to the supercell test case used in the 2016 Dynamical Core Model Intercomparison Project (DCMIP2016; Klemp et al., 2015; Ullrich et al., 2017; Zarzycki et al., 2019). The DCMIP2016 supercell test case was conducted on a small Earth with the radius reduced by a factor of 120 and no rotation. In contrast, our simulations are conducted on a full-size Earth. Figure 1 shows examples of the grid configurations used in this study (more details can be found in Section 2). Our model uses grid-stretching techniques of Schmidt (1977) and Harris et al. (2016), which can reach cloud-resolving scales while requiring less than one one-thousandth of the computational resources that would be needed for the simulation to be performed at the same resolution globally.

FV3-based models have long demonstrated their strengths in simulating supercells at 3–4 km grid spacings, at which supercell thunderstorms are marginally resolved (Potvin & Flora, 2015; Verrelle et al., 2015). This has been demonstrated in the GFDL experimental global-nest model Continental System for High-resolution prediction on Earth-to-Local Domains (C-SHiELD; Kaltenbaugh et al., 2022; Harris et al., 2019) and the pre-operational Rapid Refresh Forecasting System (RRFS; Degelia et al., 2023). While those models are capable of simulating supercells, they have too coarse of a grid spacing to simulate fine-scale dynamical structures within the supercells. As a part of the supercell's circulation, those fine-scale structures themselves also modulate the supercell's circulation. Better simulation of those fine-scale structures leads to better forecasts of supercells (Potvin & Flora, 2015).

The proposed model can simulate individual supercells and even intriguing vortices that develop near the ground and are qualitatively similar to tornadoes. We refer to those vortices as “tornado-like vortices (TLVs),” analogous to the “tropical cyclone-like vortices” in 20–100 km global models (e.g., Chen & Lin, 2013; Zhao et al., 2012). We believe that this is the first time such vortices have ever been simulated at kilometer scales in a full-size Earth global model. These simulations underscore the capability of the FV3 on cloud-resolving scales and open the opportunity to study cross-scale interactions of convective severe weather.

2. Model Description and Simulation Design

An idealized nonhydrostatic global model that can reach the cloud-resolving scale locally is developed for this study. The model utilizes FV3, which solves the vector-invariant Euler equations for atmospheric motions using the C-D grid algorithm of Lin and Rood (1997) on a gnomonic cubed-sphere grid (Putman & Lin, 2007) and a Lagrangian vertical coordinate (Lin, 2004). The pressure gradient force is solved by the finite-volume algorithm

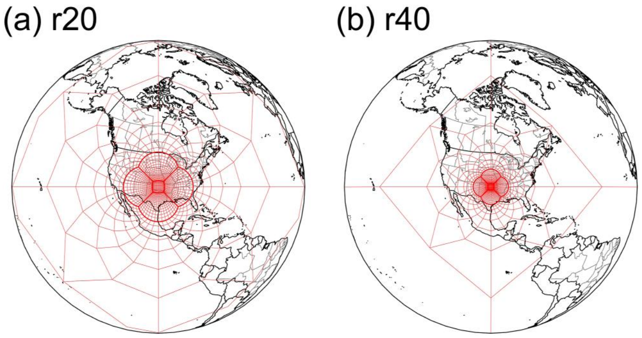

Figure 1. Illustration of two stretched grid configurations for a C512 cubed-sphere grid. Grids are shown by light red lines and the cubed-sphere edges are shown by heavy red lines. Each grid box represents 32 by 32 actual grid cells. (a) r20 configuration, the finest grid spacing is about 1 km; (b) r40, ~500 m. Coastlines and political boundaries are plotted for reference.

Table 1
Configuration and Wall-Clock Time for Each 2-hr Simulation

Resolution (km)	Cubed-sphere resolution	Grid-stretching factor	Dynamics timestep (s)	CPU cores	Wall time (s)
4	128	20	5.0	24	893
2	256	20	2.5	96	1,372
1	512	20	1.25	384	2,832
0.5	512	40	0.625	384	3,834

Note. The wall-clock time is a median calculated from five realizations.

of Lin (1997). The nonhydrostatic component is handled by a vertically semi-implicit scheme described in Harris et al. (2020). For physics parameterization, we use the GFDL microphysics scheme, version 3 (Zhou et al., 2022) with warm-rain processes only for simplicity, following the supercell test case proposed in DCMIP2016. The GFDL microphysics scheme has been previously used in the study of anvil cloud fraction (Jeevanjee & Zhou, 2022). They found that the warm-rain only and the full microphysics produce similar cloud structures.

FV3 can refine the cubed-sphere grid by an analytical “stretching” (Harris et al., 2016; Schmidt, 1977) that attracts grid points to a specified central location. The transformation of the latitude, with respect to the specified central location as if it is the South Pole, from θ (latitude) to Φ (latitude relative to the specified central location) is given by

$$\sin(\Phi) = \frac{D + \sin(\theta)}{1 + D\sin(\theta)} \text{ with } D = \frac{1 - c^2}{1 + c^2}, \tag{1}$$

where c is the stretching factor. The resulting grid can then be rotated so the high-resolution region is over the area of interest. Equation 1 describes a smooth, analytic way to generate variable-resolution grids by stretching grids on a globe. Such stretched grids have been used extensively in a variety of different applications to refine to convection-allowing and storm-resolving scales (e.g., Harris et al., 2019; Zhou et al., 2019). For this study, four configurations of the cubed-sphere grid are used to achieve different horizontal resolutions. A cubed-sphere with 128×128 (C128) and 256×256 (C256) cells on each face is stretched by a factor of 20 to reach minimum grid-cell widths of 4 and 2 km, respectively. A cubed-sphere with 512×512 (C512) cells on each face is stretched by a factor of 20 and 40 to reach minimum grid-cell widths of 1 km and 500 m, respectively. Figure 1 shows examples of stretched C512 cubed-sphere grids in the 1 km and 500 m cases. The center of the high-resolution region is placed at 35.4°N and 262.4°W for demonstration purposes. The geography does not affect the solution as the model does not account for topography and the Earth's rotation. The grid configurations are summarized in Table 1. All simulations use 90 vertical levels with a top at 50 hPa. The vertical layer thickness is finest at the bottom level (~8 m) and gradually expands with height. The bottom boundary incorporates a free-slip boundary condition, and the top boundary enforces a constant pressure. This “flexible lid” boundary condition can greatly reduce wave reflection but cannot fully eliminate it. A sponge layer is also incorporated at the model top to reduce the wave reflection (Harris et al., 2021).

All simulations are initialized using the environment of Toy (2012) with modifications. The vertical profile of the environment is shown in Figure 2. The 0–6 km bulk wind shear is 31 $\mathrm{m{\cdot}s^{-1}}$ and the 0–3 km storm-relative helicity is 90 $\mathrm{m^2 \cdot s^{-2}}$. This quarter-circle shear profile is favorable for the development of supercells (Weisman & Rotunno, 2000). The thermodynamic profile is adapted from Weisman and Klemp (1982) and is horizontally uniform. The environment has a convective available potential energy of 2,515 $\mathrm{J{\cdot}kg^{-1}}$ and has been used extensively to study supercell thunderstorms (e.g., Lasher-Trapp et al., 2021; Markowski, 2024; Peters et al., 2020; Potvin & Flora, 2015). For the wind profile (U and V in a local Cartesian system), a piecewise approximation of Toy's profile is used:

$$U(z) = \begin{cases} -8\ \mathrm{m \cdot s^{-1}} \cos\left(\frac{\pi z}{4}\right) & \text{if } z \leq 2 \text{ km}, \\ 22\ \mathrm{m \cdot s^{-1}} \left(\frac{z-2}{4}\right) & \text{if } 2 \text{ km} < z \leq 6 \text{ km}, \\ 22\ \mathrm{m \cdot s^{-1}} & \text{if } z > 6 \text{ km}, \end{cases}$$

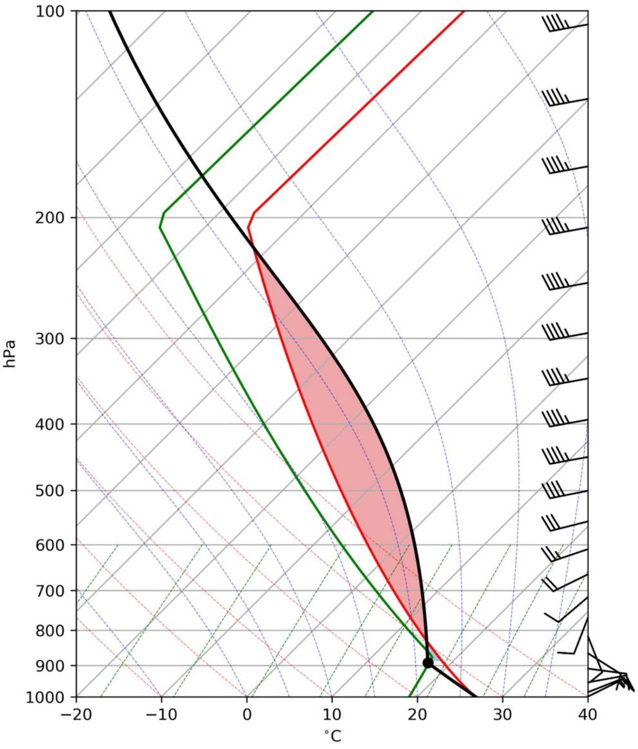

Figure 2. Skew-T plot of the initial thermodynamic and wind profiles. Temperature and dewpoint are indicated by the solid red and green curves, respectively. Black solid curve represents the temperate of a parcel rising from the surface. Black dot represents the lifting condensation level. Red shading area represents the convective available potential energy. Wind barbs are plotted in knots.

$$V(z) = \begin{cases} 8\ \mathrm{m \cdot s^{-1}}\left[\sin\left(\frac{\pi z}{4}\right) - 0.5\right] & \text{if } z \leq 2\ \mathrm{km}, \\ 4\ \mathrm{m \cdot s^{-1}} & \text{if } z > 2\ \mathrm{km}. \end{cases} \tag{2}$$

where z is the altitude in km.

The wind profile is then mapped onto a spherical domain (u and v in a spherical coordinate system) by multiplying a horizontal Gaussian:

$$u(\lambda, \theta, z) = U(z)\exp\left(-\frac{8D_{gc}}{R_e}\right), \tag{3}$$

and similarly for $v(\lambda,\ \theta,\ z)$, where λ is longitude; D_{gc} is the great-circle distance from the center of the high-resolution region; R_e is the radius of the Earth. This localization, together with the fact that we use a non-rotating earth, allows this wind field to be specified without needing to consider the spherical geometry of the earth or satisfying complex balance conditions.

The model uses a warm bubble to initiate convection. For all simulations, the thermal perturbation of the warm bubble is 2 K. The radius of the bubble is 10 km in the horizontal and 1.4 km in the vertical. All four simulations are integrated for 2 hr with the same physics timestep of 5 s. The dynamics timestep decreases with increasing resolutions to keep the integration numerically stable. The dynamics timesteps at different resolutions are tabulated in Table 1.

Table 1 also lists the number of central processing unit (CPU) cores used and the wall-clock timings for each simulation. The CPU model used in this study is Intel Xeon Gold 6148. We increase the number of the CPU cores with increasing cubed-sphere resolution to keep the simulation time manageable. Note that the wall time of the 500 m case is only about 30% more, compared to the 1 km case, even though its horizontal resolution doubles and its dynamics timestep halves. This is because both 500 m and 1 km cases use the same number of grid cells and so total amount of the computational cost for each dynamics timestep is roughly the same. Compared to other TLV simulations (Ito et al., 2024; Orf et al., 2017; Spiridonov et al., 2021; Sun et al., 2019), the computational cost of our model is at least one tenth lower, despite that the high-resolution domain used is at least 100 times larger. The highly configurable model setup and low computational cost underscore the flexibility and efficiency of the FV3 dynamical core.

3. Supercell in a Locally Refined Global Model

Our global model can simulate an individual supercell realistically at all four resolutions considered. Despite having varied horizontal resolutions, all simulated supercells show similarities in terms of storm morphology. A pioneering observational study (Byers & Braham, 1948) categorizes the life cycle of a thunderstorm into three stages: cumulus stage (characterized by updrafts and little-to-no precipitation), mature stage (characterized by both updrafts and downdrafts and precipitation), and dissipating stage (characterized by downdrafts and diminishing precipitation). In our simulations, after initialization, the supercell goes through the cumulus stage and persists in the mature stage. Figure 3 shows the appearance of the supercell in its mature stage at different resolutions. Common storm features can be seen, including protruding overshooting tops and a wide-spreading anvil (Doswell & Burgess, 1993). All simulations have a storm of similar dimensions: about 40 km in both x and y directions. The storm in each simulation can grow to a height over 15 km. Such similarity in the size is a result of the same warm bubble used to initialize the simulations. At higher resolutions, expectedly, the supercell's appearance becomes more complicated, as diabatic processes and turbulent motions at small scales are better resolved. The overshooting top (dome-like protrusion above the anvil) becomes more prominent, and the anvil shows more wave structures. Also, the supercell at a higher resolution tends to grow faster with more intense

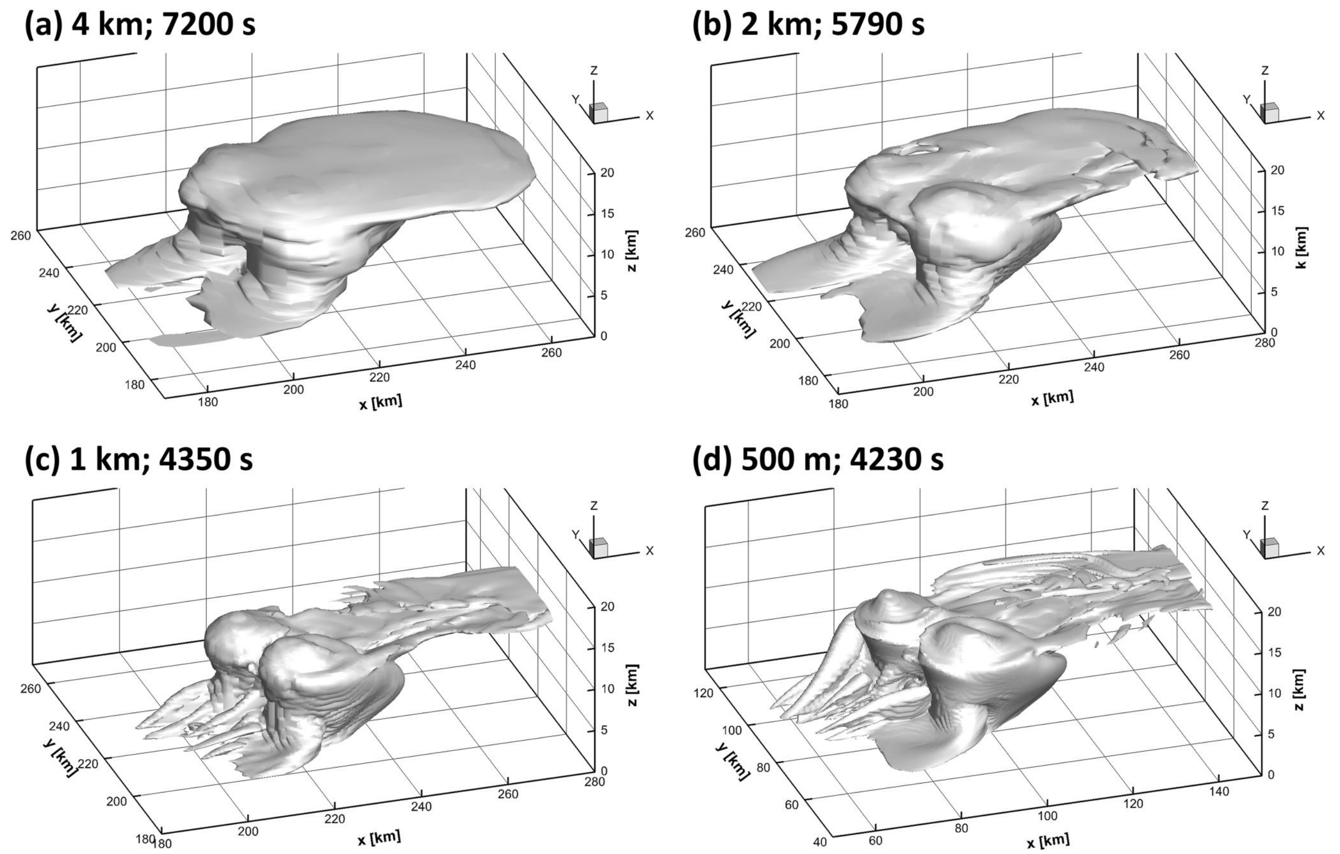

(a) 4 km; 7200 s

(b) 2 km; 5790 s

(c) 1 km; 4350 s

(d) 500 m; 4230 s

Figure 3. Perspective view of a supercell in its mature stage for the (a) 4 km, (b) 2 km, (c) 1 km, and (d) 500 m simulations. The white isosurface depicts the appearance of the supercell, which is defined by 0.1 g·kg^{-1} in total hydrometeor q_l (a combination of cloud water q_c and rainwater q_r). The x-axis, y-axis, and z-axis are directed eastward, northward, and upward, respectively. The simulation time of the snapshot is indicated.

updrafts than that at a lower resolution. Such dependencies on grid spacing are consistent with previous studies (e.g., Noda & Niino, 2003; Potvin & Flora, 2015).

At all resolutions the supercell splits, which is expected given the veering low-level wind profile. The behavior of storm splitting is consistent with previous studies using similar wind profiles (e.g., Toy, 2012; Weisman & Rotunno, 2000). At a higher resolution, the splitting occurs more quickly and prominently. One possible explanation is that the vortex dynamics and pressure perturbations are better resolved at a higher resolution, which plays an important role in the storm splitting.

Next, we examine the dynamics of the simulated supercell, focusing on the stronger, counter-clockwise-rotating right-moving cell (the southern cell in Figure 3). Figure 4 shows the horizontal distribution of vertical vorticity ζ, vertical velocity w, and q_l in all simulations. ζ and q_l are from the level near the ground (~27 m AGL), while w is from another level aloft (~1.74 km AGL). ζ and w are used to illustrate the dynamics of the supercell whereas q_l is used to depict the shape of the supercell. From q_l distribution, the supercell in all cases gets twisted by the clockwise hodograph curvature (Equation 2). At higher resolutions, the bending of the storm becomes more prominent. All simulations, except for the 4 km case, show a hook-shaped pattern, resembling the hook echo radar signature of a supercell. In particular, the hook-shaped pattern is well-resolved in the 1 km and 500 m simulations. A hook echo signature is a useful indication of tornadogenesis, as discussed by many studies (e.g., Markowski, 2002). Indeed, all simulations, except for 4 km, have a TLV forming near the ground. We will examine those vortices in detail and discuss their formation in the following section.

In addition to the hook-shaped pattern, common storm structures such as forward flank downdraft (FFD) and rear flank downdraft (RFD) can be seen in Figure 4, especially in the high-resolution simulations (1 km and 500 m). Take the 1 km simulation for example (Figure 4c), an FFD is shown by a region of strong and well-

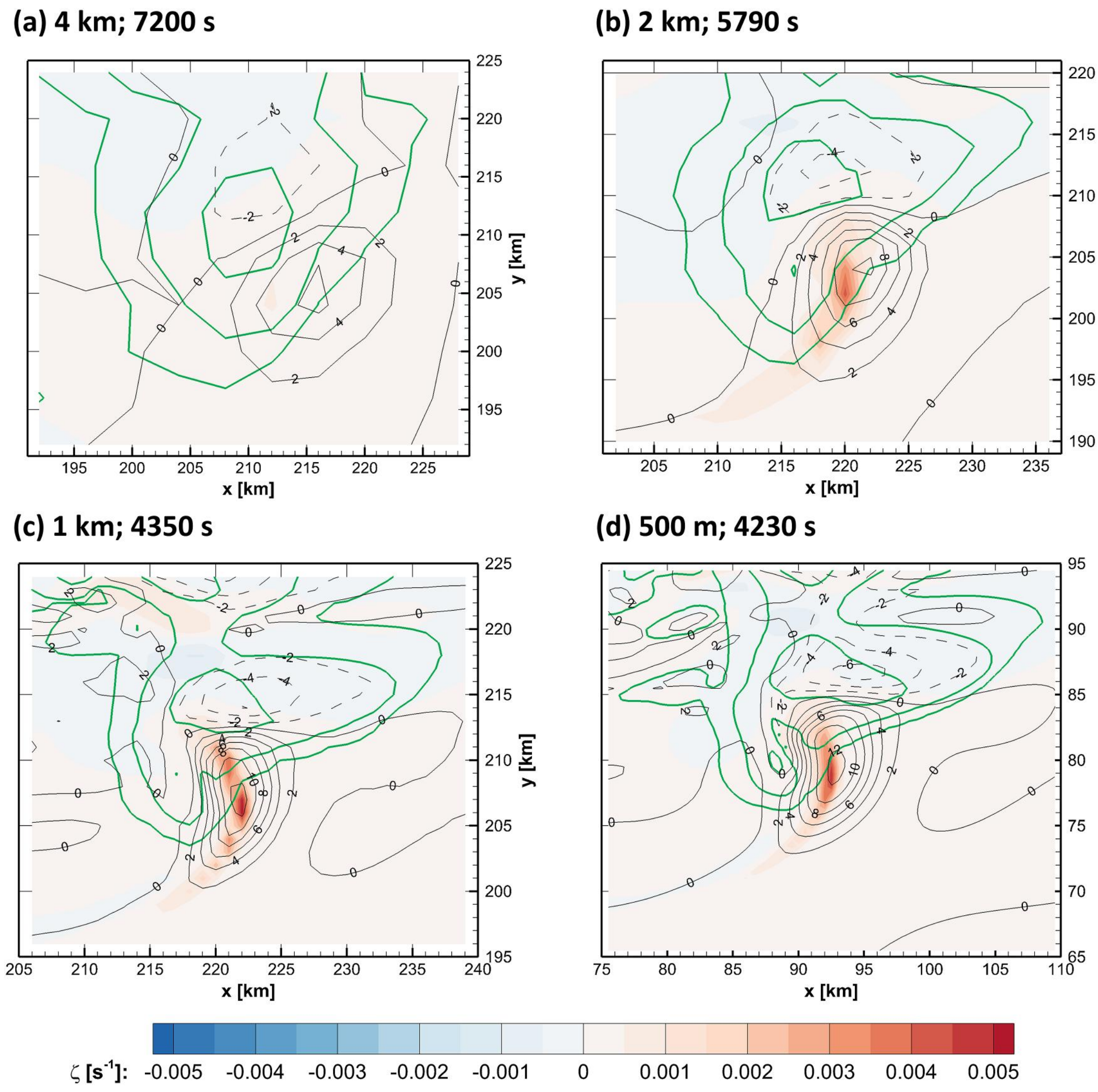

Figure 4. Dynamical structure of the counter-clockwise-rotating right-moving cell in the mature stage in (a) 4 km, (b) 2 km, (c) 1 km, and (d) 500 m simulations at the same time as in Figure 3. Color shading and green contours are ζ and q_l, respectively, near the ground (~27 m AGL). The q_l contours are 0.1, 1.0, and 5.0 g·kg^{-1}. Black contours show w at an AGL of ~1.74 km. The w contour interval is 2 m s^{-1}, with negative contours dashed.

organized downdrafts, primarily generated by precipitation loading and evaporative cooling around x = 222.5 km and y = 215.0 km, north to the main updraft at x = 222.0 km and y = 207.0 km. An RFD develops west to the main updraft around x = 210.0 km and y = 205.0 km (roughly outlined by the zero contour of w), a weak and loosely defined downdraft is forced primarily by vertical pressure gradient (Markowski & Richardson, 2010). Both FFD and RFD are stronger as the resolution increases. Previous studies suggest that RFD plays an important role in the production of tornadoes (e.g., Davies-Jones & Brooks, 1993; Markowski et al., 2002). Further information on hook echo, FFD, and RFD can be found in textbooks on cloud dynamics (e.g., Cotton et al., 2010; Houze, 2014).

The storm morphology and the dynamical features are consistent with previous observational and theoretical studies (e.g., Figure 2 in Davies-Jones, 2015). In the 4-km simulation, the overshooting top, RFD, and FFD are not as prominent as in other cases at a higher resolution. Nevertheless, the dynamics of the supercell in the 4-km simulation are qualitatively similar to that in the high-resolution ones. The result indicates that our global model is capable of reproducing a supercell storm realistically. However, a 4 km resolution only marginally resolves the supercell dynamics and is too coarse to simulate TLVs.

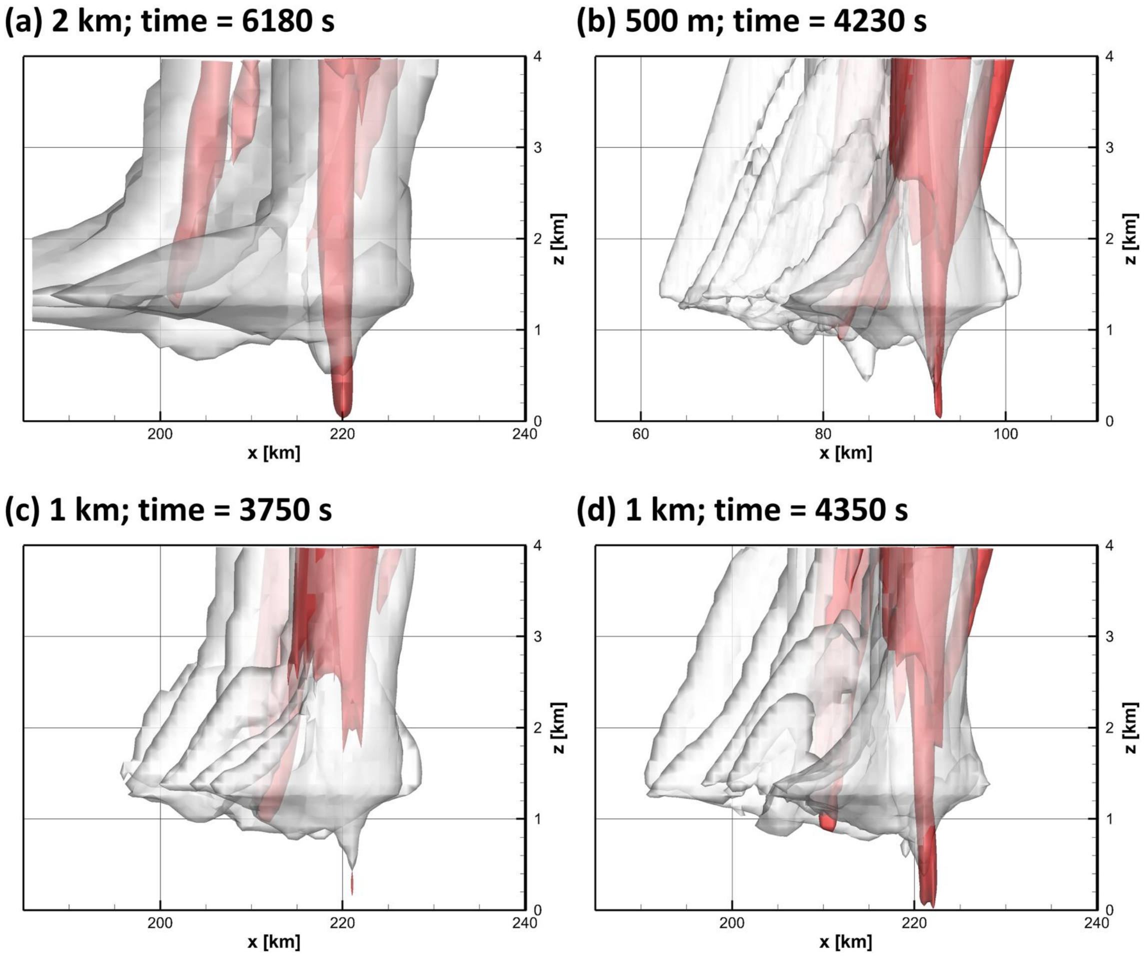

Figure 5. Three-dimensional view of cloudy TLV. (a) 6,180 s in 2 km, (b) 4,230 s in 500 m, (c) 3,750 s, and (d) 4,350 s in 1 km simulation. The solid red isosurface is $\zeta = 0.005\ \mathrm{s}^{-1}$, while the transparent white isosurface is $q_c = 0.1\ \mathrm{g{\cdot}kg}^{-1}$. The angle of view is from south to north.

4. Tornado-Like Vortex

In this section, we report and discuss the existence of an intriguing cloudy vortex that develops near the ground in all cases except for the 4 km (Figures 4 and 5). As the vortices in those three simulations are similar physically, we use the 1 km simulation only to illustrate the physics and formation of the vortex. Figure 4c shows the horizontal distribution of ζ near the ground in the 1 km simulation. A strong ζ maximum is developing locally at $x = 222.0$ km and $y = 207.0$ km, near the hook-shaped pattern in q_l discussed previously. The strong ζ is a horizontal cross-section of a three-dimensional vortex. Figures 5c and 5d show the development of the cloudy vortex near the ground. At 3,750 s into the simulation, a local, vertically extending vortex is developing at $x = 221.0$ km and $z = 0.3$ km below the downward extruding cloud (Figure 5c). The extruding cloud resembles a funnel cloud that is often, but not always, a visual precursor of a tornado (Modahl & Gray, 1971). The funnel cloud forms because the moist air near the ground (due to the evaporation of rainwater) gets lifted by the rotating updraft and condenses by adiabatic cooling, as shown in Figure 6. As time goes on, the vortex intensifies and extends both upward and downward, forming a long vortex from the ground all the way to the middle levels inside the supercell (Figure 5d). Also, the funnel cloud expands a bit. This cloudy vortex is long-lasting and evolving toward the end of the simulation. The vortex has a width of ~3 km in the 1 km simulation. The vortex in the 2 km case has a comparable size and that in the 500 m case is slightly thinner. These vortices are much wider than a typical tornado (hundreds of meters) but comparable to the widest "wedge" tornadoes, such as the 5-km wide tornado studied by Wurman et al. (2013). We refer to these cloudy vortices as TLVs hereafter, in analogy to the "tropical cyclone-like vortices" in 20–100 km global models (e.g., Chen & Lin, 2013; Zhao et al., 2012). Compared to previous TLV simulations (e.g., Markowski, 2024; Orf et al., 2017; Spiridonov et al., 2021), the

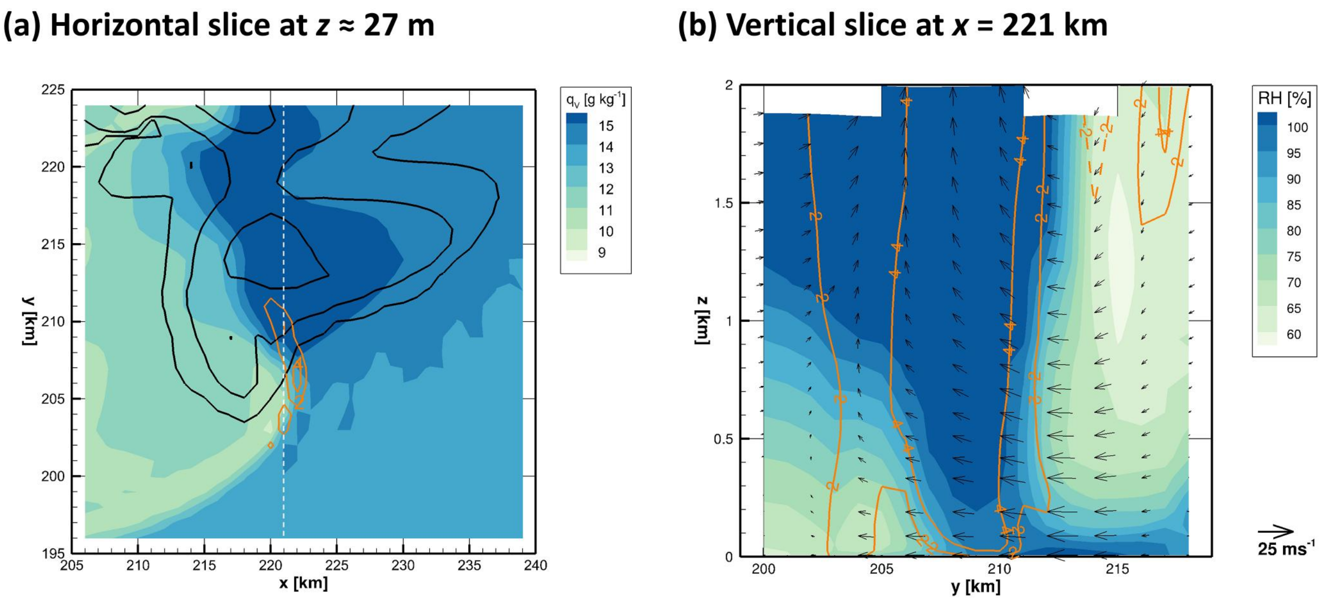
(a) Horizontal slice at $z \approx 27$ m

(b) Vertical slice at $x = 221$ km

Figure 6. Structure of cloudy vortex at 4,350 s in the 1 km simulation. (a) Horizontal cross-section near the ground ($z \sim 27$ m). q_v is plotted in color shading. Black contours represent q_l of 0.1, 1.0, and 5.0 g·kg^{-1}. Orange contours represent ζ in the unit of 0.001 s^{-1}, with negative contours dashed and zero contour omitted. White dashed line indicates the location of (b) vertical cross-section. Relative humidity (RH) is plotted in color shading. Wind vectors are plotted in black.

strength (vertical vorticity) of TLVs in our simulations is two orders of magnitude smaller. The width of TLVs in our simulations is an order of magnitude larger. The weaker and wider TLVs in our simulations are likely attributed to the difference in grid-spacing (kilometers in this study vs. O[10-m] in others). Nevertheless, the dynamical features of the TLVs (e.g., rotating updraft developed near the ground) in our simulations are consistent with previous studies.

Next, we examine the formation of the TLV through the Eulerian vertical vorticity equation. The vertical vorticity equation in height coordinates can be written as:

$$\frac{\partial \zeta}{\partial t} = -\nabla \cdot \vec{v}\zeta - \zeta\left(\frac{\partial u}{\partial x} + \frac{\partial v}{\partial y}\right) + \left(\frac{\partial w}{\partial y}\frac{\partial u}{\partial z} + \frac{\partial w}{\partial x}\frac{\partial v}{\partial z}\right) + \left(\frac{\partial p}{\partial x}\frac{\partial \alpha}{\partial y} + \frac{\partial p}{\partial y}\frac{\partial \alpha}{\partial x}\right), \tag{4}$$

where p and α are the pressure and specific density, respectively. Equation 4 describes that the local tendency of ζ is equal to, in order, advection, stretching, tilting, and baroclinicity.

We compute each of the four terms within the 1-km simulation. It turns out that the tilting and stretching terms play essential roles in forming the vortex, as has been found by numerous studies on tornadogenesis (Davies-Jones, 2015; Markowski & Richardson, 2009; Orf et al., 2017; Rotunno et al., 2017). Figure 7 shows the contribution from the tilting and stretching terms when the vortex starts to develop (the same moment as in Figure 5c). Beneath the vortex, the tilting term produces positive ζ near the ground (Figure 7a) as the gradient in vertical velocity near the updraft tilts horizontal vorticity into the vertical. This positive ζ will get transported upward by the updraft. At the same time, the stretching term acts to intensify the TLV near the ground through convergence (Figure 7b). The effects that the tilting and stretching terms have on forming the TLV are consistent with previous studies. The baroclinicity and advection do not appear to play an important role in forming the TLV through direct generation of vertical vorticity. The baroclinic term is at least one order of magnitude smaller than the tilting and stretching terms near the vortex. The advection term principally acts to move the vorticity maximum downstream. The time evolution of the vorticity budget can be found in Figure S1. One caveat is that Equation 4 may underestimate the role of baroclinity (or other mechanisms) on the formation of TLV as it cannot discriminate the source of the horizontal vorticities being tilted. A review paper written by Davies-Jones (2015) shows that baroclinity is an important source of horizontal vorticity near the ground. A recent study (Markowski, 2024) shows that a turbulent boundary layer could be an important source of horizontal vorticity, which

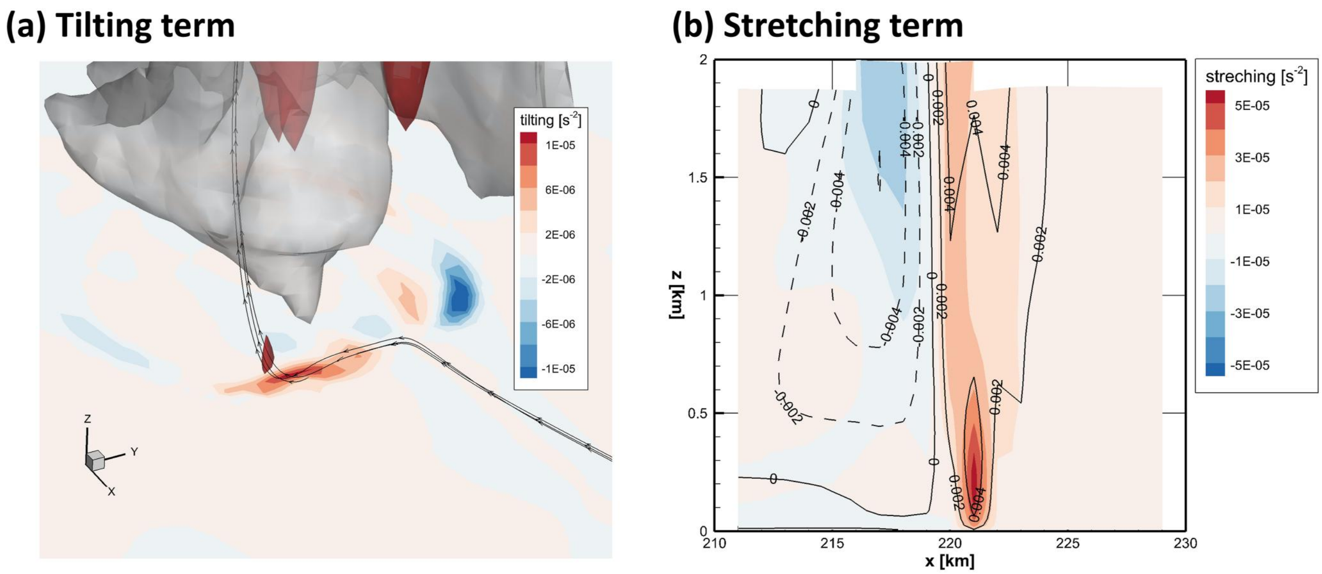

(a) Tilting term

(b) Stretching term

Figure 7. Two main contributors from the vorticity equation to the formation of the TLV when the vortex is about to develop (3,750 s) in the 1 km case. (a) A horizontal cross-section of the tilting term near the ground, $z \sim 27$ m, in a 3-dimensional view. The solid red isosurface represents the TLV (plotted by $\zeta = 0.005\ \mathrm{s}^{-1}$), while the transparent white isosurface represents the funnel cloud (plotted by $q_c = 0.1\ \mathrm{g{\cdot}kg}^{-1}$). Color shading represents the contribution from the tilting term. Streamlines through the vortex are plotted. (b) Stretching term in an xz cross-section cut through the vortex ($y = 209$ km). Color shading represents the contribution from the stretching term. Line contours show vertical vorticities, with negative contours dashed.

cannot be revealed explicitly by Equation 4. Nonetheless, the analysis of the vorticity budget shows the leading role of tilting and stretching in forming the TLVs is consistent with previous studies on tornadogenesis.

5. Conclusions and Discussion

In the above, we present numerical simulations of individual supercells and unprecedented TLVs on a full-size Earth using a newly developed idealized global model. By utilizing a stretched global grid, the model can perform simulations on cloud-resolving scales using modest computational resources. The model can produce a realistic supercell even when the supercell dynamics is marginally resolved at a 4-km grid spacing. The simulated storm morphology is consistent with observations and previous studies. Our results demonstrate a couple of interesting features of this simplified FV3-based model, including (a) that a super-stretched global grid (up to a factor of 40) remains stable and accurate; and (b) that this setup could be a useful tool for process studies without the hassle of specifying lateral boundary conditions. It also shows the value of an FV3-based model for simulation and prediction on cloud-resolving scales, which would benefit the further development of the existing FV3-based models.

We found our simulated supercells also produced cloudy TLVs, which, to the best of our knowledge, have never before been simulated in a kilometer-scale model or in any global model. While wider than typical real-world tornadoes due to our grid cell sizes, the vortex is qualitatively similar to a tornado: a funnel cloud with an intense vortex. It is found that, through analysis based on the Eulerian vertical vorticity equation, the tilting term initiates the vortices that are then intensified through stretching, indicating that the model is capturing the same dynamical processes witnessed in real tornadoes.

Previous modeling studies of tornadoes have used grid spacings of 50 m or smaller (Orf et al., 2017, and references therein). The capability of our model to produce TLVs at kilometer scales may reflect the strength of the D-grid staggering used in the FV3 dynamical core. On the D-grid, tangential winds are defined along grid boundaries, so the circulation and thus by Stokes' Theorem cell-mean vorticity can be computed exactly. Cell-mean vorticity is also co-located with vertical velocity, so their product, updraft helicity, is advected like a scalar similar to how FV3 handles potential vorticity (Lin & Rood, 1997). This may be the reason that our model can produce an intense vortex reminiscent of tornadoes even at kilometer scales, demonstrating the value of FV3's emphasis on vorticity dynamics.

The FV3 dynamical core is capable of computing dynamics and thermodynamics over a broad range of scales, ranging from planetary waves (e.g., Harris et al., 2020) to TLVs (as discussed in this paper). Our next step will be to take advantage of this capacity to study the cross-scale interactions involving supercells and tornadoes. Gensini et al. (2019) studied the teleconnection between the U.S. tornadoes and planetary circulation features that were obtained from reanalysis data. One possible way to simulate such teleconnections is to have a nest domain that is fine enough to simulate the TLVs in an existing semi-operational FV3-based convection-allowing model, such as RRFS or C-SHiELD. A well-developed FV3-based model will be well-placed to simulate multiple-scale atmospheric phenomena, which opens the opportunity to study the cross-scale interactions dynamically and, in turn, will lead to a better understanding of convective storm activity, both for storm prediction and projection under external forcing (Cheng et al., 2022).

Data Availability Statement

The model used in this study is available at https://github.com/NOAA-GFDL/SHiELD_build. Simulations presented in this study are available at Cheng (2023).

Acknowledgments

The authors thank Chih-Chi Hu for valuable discussions; editor Sara C. Pryor and two anonymous reviewers for their constructive comments. MetPy (May et al., 2022) is used to plot the Skew-T diagram (Figure 2). This study is supported under awards NA18OAR4320123, NA19OAR0220146, and NA19OAR0220147 from the National Oceanic and Atmospheric Administration (NOAA), U.S. Department of Commerce. This project is additionally funded under the NOAA Research Global-Nest initiative.

References

Bolot, M., Harris, L. M., Cheng, K.-Y., Merlis, T. M., Blossey, P. N., Bretherton, C. S., et al. (2023). Kilometer-scale global warming simulations and active sensors reveal changes in tropical deep convection. *Npj Climate and Atmospheric Science*, *6*(1), 1–8. https://doi.org/10.1038/s41612-023-00525-w

Byers, H. R., & Braham, R. R. (1948). Thunderstorm structure and circulation. *Journal of Meteorology*, *5*(3), 71–86. https://doi.org/10.1175/1520-0469(1948)005<0071:TSAC>2.0.CO;2

Chen, J.-H., & Lin, S.-J. (2013). Seasonal predictions of tropical cyclones using a 25-km-resolution general circulation model. *Journal of Climate*, *26*(2), 380–398. https://doi.org/10.1175/JCLI-D-12-00061.1

Cheng, K.-Y. (2023). Data for supercells and tornado-like vortices in an idealized global atmosphere model [Dataset]. *Zenodo*. https://doi.org/10.5281/zenodo.8428465

Cheng, K.-Y., Harris, L., Bretherton, C., Merlis, T. M., Bolot, M., Zhou, L., et al. (2022). Impact of warmer sea surface temperature on the global pattern of intense convection: Insights from a global storm resolving model. *Geophysical Research Letters*, *49*(16), e2022GL099796. https://doi.org/10.1029/2022GL099796

Cotton, W. R., Bryan, G., & van den Heever, S. C. (2010). *Storm and cloud dynamics* (2nd ed.). Academic Press.

Davies-Jones, R. (2015). A review of supercell and tornado dynamics. *Atmospheric Research*, *158–159*, 274–291. https://doi.org/10.1016/j.atmosres.2014.04.007

Davies-Jones, R., & Brooks, H. (1993). Mesocyclogenesis from a theoretical perspective. In *The tornado: Its structure, dynamics, prediction, and hazards* (pp. 105–114). American Geophysical Union (AGU). https://doi.org/10.1029/GM079p0105

Degelia, S. K., Wang, X., Wang, Y., & Johnson, A. (2023). Assimilation of GOES-16 ABI all-sky radiance observations in RRFS using EnVar: Methodology, system development, and impacts for a severe convective event. *Monthly Weather Review*, *151*(10), 2739–2758. https://doi.org/10.1175/MWR-D-23-0057.1

Doswell, C. A., III., & Burgess, D. W. (1993). Tornadoes and toraadic storms: A review of conceptual models. In *The tornado: Its structure, dynamics, prediction, and hazards* (pp. 161–172). American Geophysical Union (AGU). https://doi.org/10.1029/GM079p0161

Gensini, V. A., Barrett, B. S., Allen, J. T., Gold, D., & Sirvatka, P. (2020). The extended-range tornado activity forecast (ERTAF) project. *Bulletin of the American Meteorological Society*, *101*(6), E700–E709. https://doi.org/10.1175/BAMS-D-19-0188.1

Gensini, V. A., Gold, D., Allen, J. T., & Barrett, B. S. (2019). Extended U.S. tornado outbreak during late May 2019: A forecast of opportunity. *Geophysical Research Letters*, *46*(16), 10150–10158. https://doi.org/10.1029/2019GL084470

Harris, L., Chen, X., Putman, W., Zhou, L., & Chen, J.-H. (2021). A scientific description of the GFDL finite-volume cubed-sphere dynamical core. https://doi.org/10.25923/6nhs-5897

Harris, L. M., Zhou, L., Kaltenbaugh, A., Clark, S., Cheng, K.-Y., & Bretherton, C. (2023). A global survey of rotating convective updrafts in the GFDL X-SHiELD 2021 global storm resolving model. *Journal of Geophysical Research: Atmospheres*, *128*(10), e2022JD037823. https://doi.org/10.1029/2022JD037823

Harris, L. M., Zhou, L., Lin, S.-J., Chen, J.-H., Chen, X., Gao, K., et al. (2020). GFDL SHiELD: A unified system for weather-to-seasonal prediction. *Journal of Advances in Modeling Earth Systems*, *12*(10), e2020MS002223. https://doi.org/10.1029/2020MS002223

Harris, L. M., Lin, S.-J., & Tu, C. (2016). High-resolution climate simulations using GFDL HiRAM with a stretched global grid. *Journal of Climate*, *29*(11), 4293–4314. https://doi.org/10.1175/JCLI-D-15-0389.1

Harris, L. M., Rees, S. L., Morin, M., Zhou, L., & Stern, W. F. (2019). Explicit prediction of continental convection in a skillful variable-resolution global model. *Journal of Advances in Modeling Earth Systems*, *11*(6), 1847–1869. https://doi.org/10.1029/2018MS001542

Houze, R. A. (2014). *Cloud dynamics* (2nd ed., Vol. 104). Academic Press.

Ito, J., Niino, H., & Tochimoto, E. (2024). Numerical simulation of tornadoes in a mini-supercell associated with Typhoon Tapah on 22 September 2019. *Journal of the Meteorological Society of Japan Series II*, *102*(2), 185–208. https://doi.org/10.2151/jmsj.2024-009

Jeevanjee, N., & Zhou, L. (2022). On the resolution-dependence of anvil cloud fraction and precipitation efficiency in radiative-convective equilibrium. *Journal of Advances in Modeling Earth Systems*, *14*(3), e2021MS002759. https://doi.org/10.1029/2021MS002759

Judt, F., Klocke, D., Rios-Berrios, R., Vanniere, B., Ziemen, F., Auger, L., et al. (2021). Tropical cyclones in global storm-resolving models. *Journal of the Meteorological Society of Japan Series II*, *99*(3), 579–602. https://doi.org/10.2151/jmsj.2021-029

Kaltenbaugh, A., Harris, L., Cheng, K.-Y., Zhou, L., Morin, M. J., & Stern, W. F. (2022). Using GFDL C-SHiELD for the prediction of convective storms during the 2021 spring and summer. In *NOAA Technical Memorandum OAR GFDL, 2022-002*. https://doi.org/10.25923/ednx-rm3441pp

Klemp, J. B., Skamarock, W. C., & Park, S.-H. (2015). Idealized global nonhydrostatic atmospheric test cases on a reduced-radius sphere. *Journal of Advances in Modeling Earth Systems*, *7*(3), 1155–1177. https://doi.org/10.1002/2015MS000435

Klemp, J. B., & Wilhelmson, R. B. (1978). The simulation of three-dimensional convective storm dynamics. *Journal of the Atmospheric Sciences*, *35*(6), 1070–1096. https://doi.org/10.1175/1520-0469(1978)035<1070:TSOTDC>2.0.CO;2

Lasher-Trapp, S., Jo, E., Allen, L. R., Engelsen, B. N., & Trapp, R. J. (2021). Entrainment in a simulated supercell thunderstorm. Part I: The evolution of different entrainment mechanisms and their dilutive effects. *Journal of the Atmospheric Sciences*, *78*(9), 2725–2740. https://doi.org/10.1175/JAS-D-20-0223.1

Lin, S.-J. (1997). A finite-volume integration method for computing pressure gradient force in general vertical coordinates. *Quarterly Journal of the Royal Meteorological Society*, *123*(542), 1749–1762. https://doi.org/10.1002/qj.49712354214

Lin, S.-J. (2004). A "Vertically Lagrangian" finite-volume dynamical core for global models. *Monthly Weather Review*, *132*(10), 2293–2307. https://doi.org/10.1175/1520-0493(2004)132<2293:AVLFDC>2.0.CO;2

Lin, S.-J., & Rood, R. B. (1997). An explicit flux-form semi-Lagrangian shallow-water model on the sphere. *Quarterly Journal of the Royal Meteorological Society*, *123*(544), 2477–2498. https://doi.org/10.1002/qj.49712354416

Markowski, P. M., & Richardson, Y. (2010). *Mesoscale meteorology in midlatitudes* (p. 407). Wiley- Blackwell. Royal Meteorological Society.

Markowski, P. M. (2002). Hook echoes and rear-flank downdrafts: A review. *Monthly Weather Review*, *130*(4), 852–876. https://doi.org/10.1175/1520-0493(2002)130<0852:HEARFD>2.0.CO;2

Markowski, P. M. (2024). A new pathway for tornadogenesis exposed by numerical simulations of supercells in turbulent environments. *Journal of the Atmospheric Sciences*, *81*(3), 481–518. https://doi.org/10.1175/JAS-D-23-0161.1

Markowski, P. M., & Richardson, Y. P. (2009). Tornadogenesis: Our current understanding, forecasting considerations, and questions to guide future research. *Atmospheric Research*, *93*(1), 3–10. https://doi.org/10.1016/j.atmosres.2008.09.015

Markowski, P. M., Straka, J. M., & Rasmussen, E. N. (2002). Direct surface thermodynamic observations within the rear-flank downdrafts of nontornadic and tornadic supercells. *Monthly Weather Review*, *130*(7), 1692–1721. https://doi.org/10.1175/1520-0493(2002)130<1692:DSTOWT>2.0.CO;2

May, R. M., Goebbert, K. H., Thielen, J. E., Leeman, J. R., Camron, M. D., Bruick, Z., et al. (2022). MetPy: A meteorological Python library for data analysis and visualization. *Bulletin of the American Meteorological Society*, *103*(10), E2273–E2284. https://doi.org/10.1175/BAMS-D-21-0125.1

Modahl, A. C., & Gray, W. M. (1971). Summary of funnel cloud occurrences and comparison with tornadoes. *Monthly Weather Review*, *99*(11), 877–882. https://doi.org/10.1175/1520-0493(1971)099<0877:SOFCOA>2.3.CO;2

Nesbitt, S. W., Salio, P. V., Ávila, E., Bitzer, P., Carey, L., Chandrasekar, V., et al. (2021). A storm safari in subtropical South America: Proyecto RELAMPAGO. *Bulletin of the American Meteorological Society*, *102*(8), E1621–E1644. https://doi.org/10.1175/BAMS-D-20-0029.1

Noda, A., & Niino, H. (2003). Critical grid size for simulating convective storms: A case study of the Del City supercell storm. *Geophysical Research Letters*, *30*(16). https://doi.org/10.1029/2003GL017498

Nugent, J. M., Turbeville, S. M., Bretherton, C. S., Blossey, P. N., & Ackerman, T. P. (2022). Tropical cirrus in global storm-resolving models: 1. Role of deep convection. *Earth and Space Science*, *9*(2), e2021EA001965. https://doi.org/10.1029/2021EA001965

Orf, L., Wilhelmson, R., Lee, B., Finley, C., & Houston, A. (2017). Evolution of a long-track violent tornado within a simulated supercell. *Bulletin of the American Meteorological Society*, *98*(1), 45–68. https://doi.org/10.1175/BAMS-D-15-00073.1

Peters, J. M., Morrison, H., Nowotarski, C. J., Mulholland, J. P., & Thompson, R. L. (2020). A formula for the maximum vertical velocity in supercell updrafts. *Journal of the Atmospheric Sciences*, *77*(11), 3747–3757. https://doi.org/10.1175/JAS-D-20-0103.1

Potvin, C. K., & Flora, M. L. (2015). Sensitivity of idealized supercell simulations to horizontal grid spacing: Implications for warn-on-forecast. *Monthly Weather Review*, *143*(8), 2998–3024. https://doi.org/10.1175/MWR-D-14-00416.1

Putman, W. M., & Lin, S.-J. (2007). Finite-volume transport on various cubed-sphere grids. *Journal of Computational Physics*, *227*(1), 55–78. https://doi.org/10.1016/j.jcp.2007.07.022

Rasmussen, E. N., Straka, J. M., Davies-Jones, R., Doswell, C. A., Carr, F. H., Eilts, M. D., & MacGorman, D. R. (1994). Verification of the Origins of rotation in tornadoes experiment: Vortex. *Bulletin of the American Meteorological Society*, *75*(6), 995–1006. https://doi.org/10.1175/1520-0477(1994)075<0995:VOTOOR>2.0.CO;2

Rotunno, R., Markowski, P. M., & Bryan, G. H. (2017). "Near ground" vertical vorticity in supercell thunderstorm models. *Journal of the Atmospheric Sciences*, *74*(6), 1757–1766. https://doi.org/10.1175/JAS-D-16-0288.1

Satoh, M., Stevens, B., Judt, F., Khairoutdinov, M., Lin, S.-J., Putman, W. M., & Düben, P. (2019). Global cloud-resolving models. *Current Climate Change Reports*, *5*(3), 172–184. https://doi.org/10.1007/s40641-019-00131-0

Schlesinger, R. E. (1978). A three-dimensional numerical model of an isolated thunderstorm: Part I. Comparative experiments for variable ambient wind shear. *Journal of the Atmospheric Sciences*, *35*(4), 690–713. https://doi.org/10.1175/1520-0469(1978)035<0690:ATDNMO>2.0.CO;2

Schmidt, F. (1977). Variable fine mesh in the spectral global models. *Beiträge Zur Physik Der Atmosphäre*, *50*, 211–217.

Spiridonov, V., Ćurić, M., Velinov, G., & Jakimovski, B. (2021). Numerical simulation of a violent supercell tornado over Vienna airport initialized and initiated with a cloud model. *Atmospheric Research*, *261*, 105758. https://doi.org/10.1016/j.atmosres.2021.105758

Stevens, B., & Bony, S. (2013). What are climate models missing? *Science*, *340*(6136), 1053–1054. https://doi.org/10.1126/science.1237554

Stevens, B., Satoh, M., Auger, L., Biercamp, J., Bretherton, C. S., Chen, X., et al. (2019). DYAMOND: The DYnamics of the atmospheric general circulation modeled on non-hydrostatic domains. *Progress in Earth and Planetary Science*, *6*(1), 61. https://doi.org/10.1186/s40645-019-0304-z

Sun, Z., Xue, M., Zhu, K., & Zhou, B. (2019). Prediction of an EF4 supercell tornado in Funing, China: Resolution dependency of simulated tornadoes and their structures. *Atmospheric Research*, *229*, 175–189. https://doi.org/10.1016/j.atmosres.2019.06.019

Toy, M. D. (2012). A supercell storm simulation using a nonhydrostatic cloud-resolving model based on a hybrid isentropic-sigma vertical coordinate. *Monthly Weather Review*, *141*(4), 1204–1215. https://doi.org/10.1175/MWR-D-12-00215.1

Ullrich, P. A., Jablonowski, C., Kent, J., Lauritzen, P. H., Nair, R., Reed, K. A., et al. (2017). DCMIP2016: A review of non-hydrostatic dynamical core design and intercomparison of participating models. *Geoscientific Model Development*, *10*(12), 4477–4509. https://doi.org/10.5194/gmd-10-4477-2017

Verrelle, A., Ricard, D., & Lac, C. (2015). Sensitivity of high-resolution idealized simulations of thunderstorms to horizontal resolution and turbulence parametrization. *Quarterly Journal of the Royal Meteorological Society*, *141*(687), 433–448. https://doi.org/10.1002/qj.2363

Wang, P. K., Cheng, K.-Y., Setvak, M., & Wang, C.-K. (2016). The origin of the gullwing-shaped cirrus above an Argentinian thunderstorm as seen in CALIPSO images. *Journal of Geophysical Research: Atmospheres*, *121*(7), 2015JD024111. https://doi.org/10.1002/2015JD024111

Weisman, M. L., & Klemp, J. B. (1982). The dependence of numerically simulated convective storms on vertical wind shear and buoyancy. *Monthly Weather Review*, *110*(6), 504–520. https://doi.org/10.1175/1520-0493(1982)110<0504:TDONSC>2.0.CO;2

Weisman, M. L., & Rotunno, R. (2000). The use of vertical wind shear versus helicity in interpreting supercell dynamics. *Journal of the Atmospheric Sciences*, *57*(9), 1452–1472. https://doi.org/10.1175/1520-0469(2000)057<1452:TUOVWS>2.0.CO;2

Wurman, J., Dowell, D., Richardson, Y., Markowski, P., Rasmussen, E., Burgess, D., et al. (2012). The second verification of the Origins of rotation in tornadoes experiment: VORTEX2. *Bulletin of the American Meteorological Society*, *93*(8), 1147–1170. https://doi.org/10.1175/BAMS-D-11-00010.1

Wurman, J., Kosiba, K., Robinson, P., & Marshall, T. (2013). The role of multiple-vortex tornado structure in causing storm researcher fatalities. *Bulletin of the American Meteorological Society*, *95*(1), 31–45. https://doi.org/10.1175/BAMS-D-13-00221.1

Zarzycki, C. M., Jablonowski, C., Kent, J., Lauritzen, P. H., Nair, R., Reed, K. A., et al. (2019). DCMIP2016: The splitting supercell test case. *Geoscientific Model Development*, *12*(3), 879–892. https://doi.org/10.5194/gmd-12-879-2019

Zavadoff, B. L., Gao, K., Lopez, H., Lee, S.-K., Kim, D., & Harris, L. M. (2023). Improved MJO forecasts using the experimental global-nested GFDL SHiELD model. *Geophysical Research Letters*, *50*(6), e2022GL101622. https://doi.org/10.1029/2022GL101622

Zhao, M., Held, I. M., & Lin, S.-J. (2012). Some counterintuitive dependencies of tropical cyclone frequency on parameters in a GCM. *Journal of the Atmospheric Sciences*, *69*(7), 2272–2283. https://doi.org/10.1175/JAS-D-11-0238.1

Zhou, L., Harris, L., Chen, J.-H., Gao, K., Guo, H., Xiang, B., et al. (2022). Improving global weather prediction in GFDL SHiELD through an upgraded GFDL cloud microphysics scheme. *Journal of Advances in Modeling Earth Systems*, *14*(7), e2021MS002971. https://doi.org/10.1029/2021MS002971

Zhou, L., Lin, S.-J., Chen, J.-H., Harris, L. M., Chen, X., & Rees, S. L. (2019). Toward convective-scale prediction within the next generation global prediction system. *Bulletin of the American Meteorological Society*, *100*(7), 1225–1243. https://doi.org/10.1175/BAMS-D-17-0246.1